Cold Regions Science and Technology 125 (2016) 162–176

Contents lists available at ScienceDirect

Cold Regions Science and Technology

journal homepage: www.elsevier.com/locate/coldregions

Four decades of observations from NGI's full-scale avalanche test site Ryggfonn—Summary of experimental results

Peter Gauer*, Krister Kristensen

Norwegian Geotechnical Institute, Norway

ARTICLE INFO

Article history:
Received 8 September 2015
Received in revised form 12 February 2016
Accepted 13 February 2016
Available online 23 February 2016

Keywords:
Snow avalanche dynamics
Full-scale tests
Measurements
Runout
Velocity
Impact pressure

ABSTRACT

The Norwegian Geotechnical Institute (NGI) has run full-scale avalanche experiments at the Ryggfonn test-site in Western-Norway for close to 40 years. The construction of an avalanche catching dam in 1981 laid the cornerstone of the so-called "Ryggfonn project". Over these years of operation, various kinds of instrumentation and structures have been placed along the avalanche path to gain in-depth understanding of avalanche dynamics and the interaction of avalanches with structures. Avalanche measurements provide benchmarks for the development and calibration of numerical avalanche models. Increasingly, these models are used for hazard zoning to estimate runout distances or impact pressures with varying return periods for assessing endangered areas. However, these models are imperfect and require a high degree of expert judgment for specifying the required model parameters. At this point, it is valuable to have reference events to evaluate simulation results.

In this paper, we summarize runout, velocity, and impact pressure observations from the Ryggfonn test site as well as some derived quantities such as the retarding acceleration or density estimates. We try to relate the measurements to ambient (in-situ) conditions during the events. For Ryggfonn, the runout observations suggest a 10 to 15% increase in runout distance comes along with a decrease of a factor 10 in probability. The expected front velocity of an avalanche as it enters the runout area at Ryggfonn is about $27 \pm 10\ \mathrm{ms}^{-1}$, but may reach $50\ \mathrm{ms}^{-1}$. The impact pressures at the beginning of the runout area are typically of the order of 100 kPa, but may reach several hundred kPa. Observations from a power line assembly give some insight in the vertical pressure distribution and its dependency of the avalanche velocity. The combination of these measurements provides some implications for the avalanche density suggesting a range of flowing densities. Our observations affirm a dependency of dynamical parameters on the ambient conditions, which were made at other locations.

1. Introduction

In many mountainous areas with seasonal or year round snow cover, snow avalanches are spectacular natural phenomena. However, avalanches constitute a deadly threat if humans or animals come in their way. Recorded history chronicles recurring catastrophic avalanche cycles with many fatalities and events that have even destroyed whole villages. Fig. 1 shows an example from Lourtier, Switzerland, during the avalanche cycle of February 1999, which affected large parts of the Alps (Gruber and Margreth, 2001; Heumader, 2000; Rapin and Ancey, 2000).

In many countries, hazard zoning and extensive construction of mitigation measures (such as supporting structures in the starting zones or avalanche dams in the runout areas), which were increasingly implemented in the second half of the last century, have reduced the number of fatalities in settlements and on roads. In countries that are lagging behind with the implementation of this kind of measures, for whatever reason, the death toll from avalanches is periodically high, as a recent example from Afghanistan in February 2015 shows ("Avalanches kill more than 300 in Afghanistan", The Telegraph, 2015).

Norway too has a long and tragic history with avalanche accidents (Furseth, 2006) and snow avalanches are one of the most frequent and deadly natural hazards in the country. Just in the last 40 years (1972–2014), avalanches have claimed 44 lives, either on roads or in houses. This number does not include those who died in the backcountry working or during recreational activities. Following a number of serious accidents in the 1960s and early 1970s, The

* Corresponding author at: Norwegian Geotechnical Institute, Sognsveien 72, N-0855 Oslo, Norway. Tel.: +47 45274743; fax: +47 22020448.
E-mail address: peter.gauer@ngi.no (P. Gauer).

http://dx.doi.org/10.1016/j.coldregions.2016.02.009

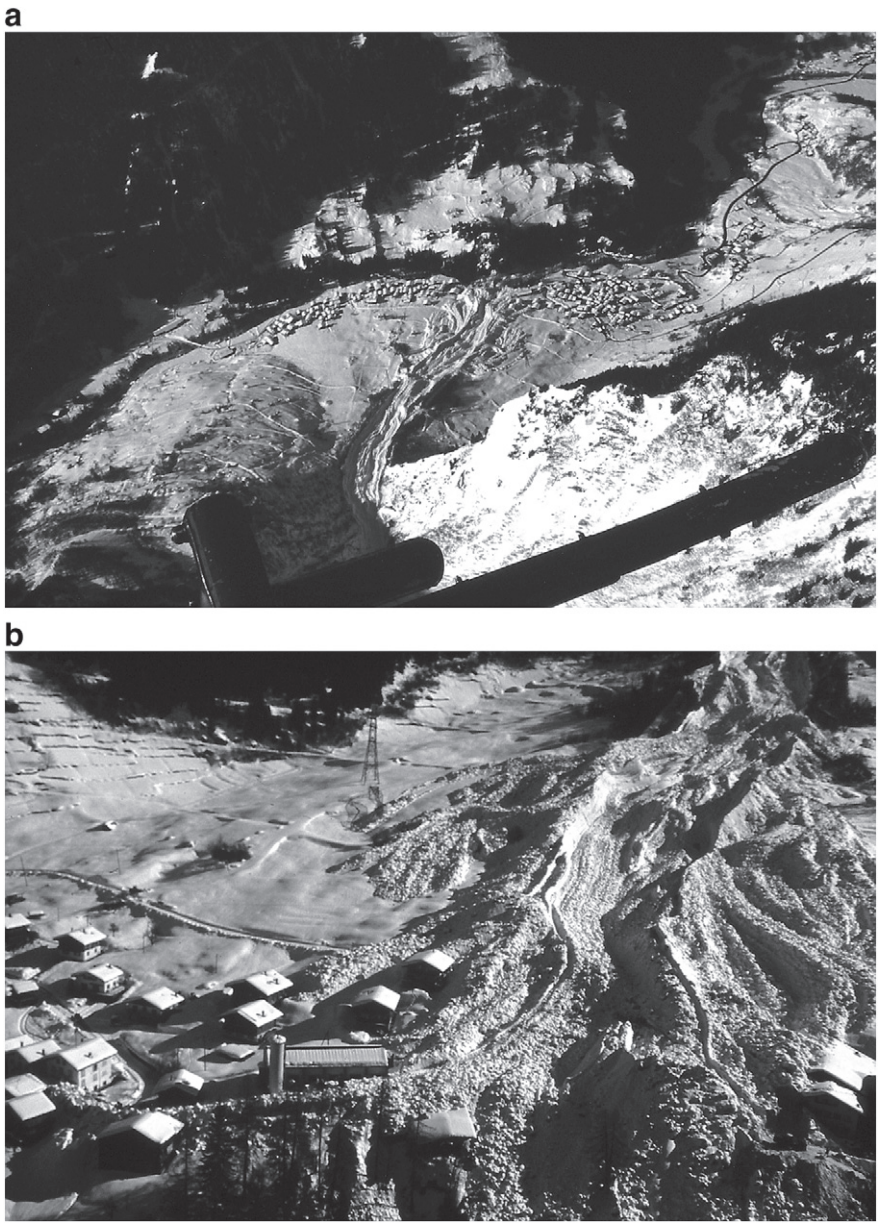

Fig. 1. Several avalanches from Bec des Rosses (3723 m a.s.l.) hit the village Lourtier (1075 m a.s.l.), Switzerland, on 20–21 February 1999. Miraculously, these avalanches caused no fatalities. Large parts of the orographic left hand side of the alluvial fan were impacted by the powder part of at least one of these avalanches.

Norwegian Parliament designated the Norwegian Geotechnical Institute (NGI) as the center of expertise on snow and avalanche research in Norway in 1972. The importance of establishing a field research station was emphasized by the parliament (Stortingsmelding Nr. 9 1972-73 Innst. S. nr. 68, 1973). With that in mind, NGI established the snow research station Fonnbu (Jaedicke et al., 2008) and the nearby full-scale avalanche test-site Ryggfonn (RGF). The official start of "The Ryggfonn Project" was in 1981, although, first preparations for artificial avalanche releases at the site were already done in 1972. The first successful release with recorded measurements was performed on 25 February 1975 (Tøndel, 1977). The aim of the test-site, was and still is, to gain in-depth understanding of avalanche flow dynamics, which is a prerequisite for effective hazard zoning and the design of protection measures.

The main focus of this paper is to provide practitioners and model developers a set of reference data. To this end, we provide a summary of observations and measurements from the Ryggfonn test-site recorded over the last 40 years. We focus on runout, velocity, and impact pressure observations as well as some derived quantities. The outcomes are organized from simple to more complicated, that is, we start with observations that are directly based on the field observations, such as volume, runout, and the corresponding probabilities and end with derived quantities, like density profiles, that require the combination of various single observations to obtain a consistent result. As far as possible, we try to link the measurements to the snow and weather conditions during the events.

2. The research infrastructure

The full-scale avalanche test-site Ryggfonn in Western-Norway (61.96 N, 7.275 E) can be compared with test sites of various sizes around the world. An overview of the (European) avalanche test sites can be found in Issler (1999) and Barbolini and Issler (2006). In addition, one can find some information on specific sites, e.g., in Ammann (1999), Maggioni et al. (2012), and Thibert et al. (2015).

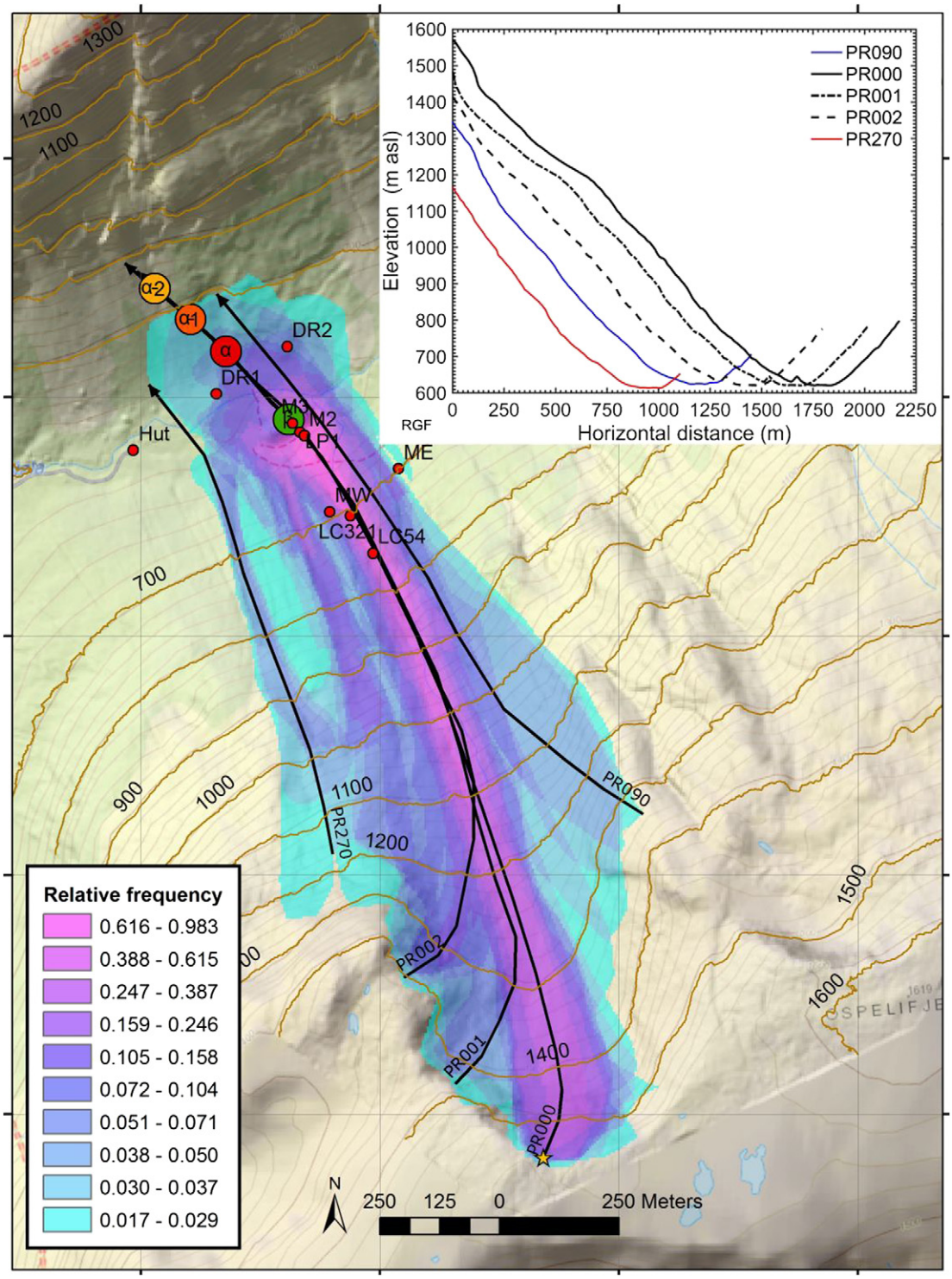

Fig. 2. Ryggfonn avalanche path. Colors indicate the relative frequency of the observed avalanche passages (based on total of 59 observations). As reference the β and the so-called α, α-1, and α-2 points of the well known α-β model (Lied and Bakkehøi, 1980) are shown. The small red dots mark some of the instrumented locations. The inset shows the marked profiles. (For interpretation of the references to color in this figure legend, the reader is referred to the web version of this article.)

Ryggfonn is one of only two operational full-scale test sites in the world where avalanches size 4 in the Canadian Avalanche Size Classification (i.e. typical mass 10^7 kg or typical path length 2000 m) can be triggered and investigated under, more or less, controlled conditions. Avalanches of size 4 are characterized by *"Could destroy a railway car, large truck, several buildings or forest with an area up to 4 hectares (ha)"* (McClung and Schaerer, 2006, Table D.1). Therefore, avalanches of this size and larger are most relevant with respect to hazard zoning. Nonetheless, size 3 avalanches have already serious destructive potential.

Fig. 2 provides an overview of the Ryggfonn avalanche path. The upper half of the north-facing track is a cirque with the main starting zone at the upper end. In addition, several release areas to the left and right of the main track (PR000) also drain into the common

Table 1
Historical summary of the operation of the Ryggfonn test site.

Date	Installation and changes
1974	First trials with placed explosives in the main release area
1975-02-25	First successful artificial avalanche release with measurements
1981 autumn	Construction of a 16 m high catching dam in the runout area
1982-04-20	First measurements of an avalanche hitting the catching dam
1983	Construction of a concrete wedge with 3 load plates (LC321) each with an area of $H \times W = 1.2 \times 0.6$ m^2; installation of a transmission line assembly (ME and MW) with tension sensors (SC321) in the lines; 6 m-mast on dam crown with a pressure sensor and strain gauges
1984	Construction of a 26 m high Y-shape power line mast, with strain gauges, accelerometer, and maximum pressure sensors
1990-04-01	A large avalanche destroyed the transmission line assembly, and tore down the Y-mast and the 6-m mast on the dam crown
1990	The Y-mast was shortened and rearranged as a 10 m high pylon; the mast on the dam was replaced
1993-02-04	The 10 m pylon was torn down
1993-03-27	The mast on the dam was torn down
1994	Pylon was shortened to 8.5 m and reerected
1997-04-17	First pulsed Doppler radar measurements by BFW-Innsbruck
2000-02-17	The pylon was destroyed once again and it damaged the concrete wedge downstream severely.
2001	The pylon was shortened once more (now 5.5 m high) and reerected and equipped with two load plates (LC54, $H \times W = 1.2 \times 0.6$ m^2).
2002	Two load plates (LP1 and LP2, $H \times W = 1 \times 1$ m^2) were mounted on the upstream side of the catching dam
2009	Two new masts M2 (15 m) and M3 (6 m) were built in front and on top of the catching dam
2011	Installation of a Wyssen avalanche tower

runout area. The profiles of the most frequent tracks are shown in the inset. The total vertical drop height of the main path is about 900 m and the horizontal runout distances typically range between 1500 and 1850 m with a maximum up to 2100 m. The β-angle of the main track is about 29° and might be regarded as mean slope angle. It is measured from the point where the tangent to the profile drops below 10° to the top of the starting zone (Lied and Bakkehøi, 1980). The track itself is slightly channeled. Typical avalanche masses range from 10^5 to 10^7 kg, but may reach up to 10^8 kg. An avalanche catching dam in the runout area makes the Ryggfonn facility unique. It is the only place where the efficiency of this kind of an avalanche mitigation measure is studied in full-scale. The β-angle was determined from the original terrain, before the dam was built.

Table 1 summarizes the history of the test site and gives an impression of the difficulties to obtain consistent measurements over a long period. More detailed description of the present-day instrumentation can be found in Gauer et al. (2010a).

3. Data

3.1. Avalanche data

In the following, we focus on observations and measurements from Ryggfonn during the last four decades. As indicated above, due to the changes in instrumentation and the often destructive conditions during the events, the quality of the data may vary. Nonetheless, they give reliable trends. Records comprise around 160 naturally released avalanches and about 30 artificially released ones. For this analysis, we used approximately 40 avalanches, which had sufficient observations, as core data. Most of the experiments at the site are documented in reports: (Gauer and Kristensen, 2004, 2005; Kristensen, 1996, 1997, 2001; Lied, 1984; Norem, 1995; Norem and Kristensen, 1985, 1986a,b; Norem et al., 1988a,b, 1989, 1991).

3.2. Meteorological data

The closest weather station to Ryggfonn is at the nearby snow research station Fonnbu, located 4.5 km north east from the test site. Unfortunately, the weather records from Fonnbu are incomplete or lacking for parts of the considered period. Therefore, we supplement these data with data derived from **seNorge** (Saloranta, 2012). The **seNorge** snow model operates with 1 × 1 km resolution. It uses gridded observations of daily air temperature and precipitation as input forcing, and simulates snow water equivalent (SWE) and snow depth (HS), among other factors. Although comparison between the available measurements from Fonnbu and the data from **seNorge** suggests a reasonable consistency, one has to keep the basic difference between the two data sets in mind. The first one provides point measurements whereas **seNorge** provides spatial averages based on assimilation of data from mostly low elevation weather stations.

In the following, we use the air temperature measured at the Fonnbu station, which are supplemented with "corrected" data from **seNorge** (i.e. the correlation between Fonnbu data and data from **seNorge** was used to complement missing data). We, specifically, consider the mean air temperature, T_a, of a 48 h period around the avalanche event. This period may also embrace episodes with temperatures above zero degrees, which may have had major effects on the snow properties. Furthermore, we refer directly to the three-day new-snow water equivalent HNW_{3d} obtained from **seNorge** for a model elevation corresponding to the release area of Ryggfonn (≈ 1600 m a.s.l.), partly adjusted with measurements from Fonnbu using the correlation between Fonnbu data and data from **seNorge**. Fig. 3 provides a brief overview of these data for the events that we have analyzed in more detail. The figure gives an impression of the distribution of the temperature and precipitation that influenced the avalanche measurements.

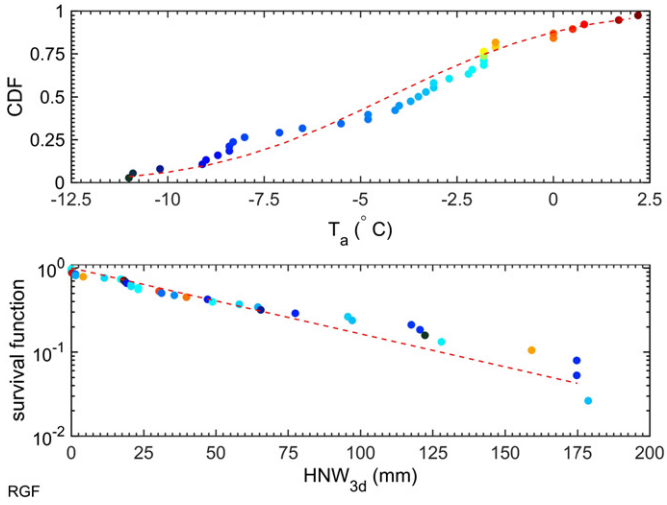

Fig. 3. Cumulative distribution function of the mean air temperature, T_a, of a 48 h period around the avalanche event (top panel) and the survival function (1-CDF) of the three-day new-snow water equivalent, HNW_{3d} for Ryggfonn (RGF) (bottom panel). Color coding reflects the air temperature. (For interpretation of the references to color in this figure, the reader is referred to the web version of this article.)

4. Observations and measurements

4.1. Avalanche volume

During field campaigns, the volumes of the avalanche deposition (V_{Dep}) were measured by traditional surveying methods or more recently, using terrestrial lidar scanning, or they were estimated based on expert judgment. The volumes of the observed/surveyed avalanches involve about three orders of magnitude ranging from about 10^3 to 475×10^3 m^3. The estimated error is of the order of ±10%. Fig. 4 shows the boxplot of the avalanche size $\log_{10}(V_{Dep}/V_0)$. Here, $V_0 = 10^3$ m^3 is chosen as a reference volume.

To give an impression how snow and weather conditions may influence the avalanche size, Fig. 5 displays the order of magnitude of the deposition volume, $\log_{10}(V_{Dep}/V_0)$, vs. air temperature, T_a, and three-day new-snow water equivalent, HNW_{3d}. Looking at the Spearman rank correlation, there is almost no correlation between $\log_{10}(V_{Dep}/V_0)$ and T_a ($\rho_{xy,z} \approx 0.07$, where $\rho_{xy,z}$ is the partial correlation controlling for HNW_{3d}) and a rather weak correlation between $\log_{10}(V_{Dep}/V_0)$ and HNW_{3d} ($\rho_{xy,z} \approx 0.33$, where $\rho_{xy,z}$ is the partial correlation controlling for T_a). The weak correlation between the avalanche size and the new-snow amount might be explained by the fact that the new-snow is only one part of the available mass as it does not account for the depth of old-snow layers or snow-drifts that formed the initial volume nor for the snow that was entrained during the avalanches descent.

4.2. Observed runout patterns

Fig. 2 shows the relative frequency (= counts/total counts) of the areas overrun by the avalanches that were surveyed during the last 40 years. Minor events, which stopped in the upper part of the track, were not always recorded and these exemptions may cause a slight bias. The affected area was either determined from visual observations of the deposits or from photos or videos. The presented perimeters may also include areas that were overrun by a powder cloud without leaving very distinctive traces. For comparison the so-called α, α-1, and α-2 points of the well known α-β model are shown (Lied and Bakkehøi, 1980). Despite the presence of the catching dam, several avalanches reached α-1, at least their powder clouds did.

Fig. 6 presents the nominal return period (i.e. the calculated return period based on the observed runout probability during the observation period) for a raster point to be reached by an avalanche/covered by deposits. Here, we used the survey data of the observed deposits, which may cause some inconsistencies as one may expect the nominal return period for an avalanche to be lower as one goes up the track. This inconsistency is caused by the fact that we only consider areas of the surveyed deposits in the runout area, since observations of the upper track were often impossible due to weather and visibility.

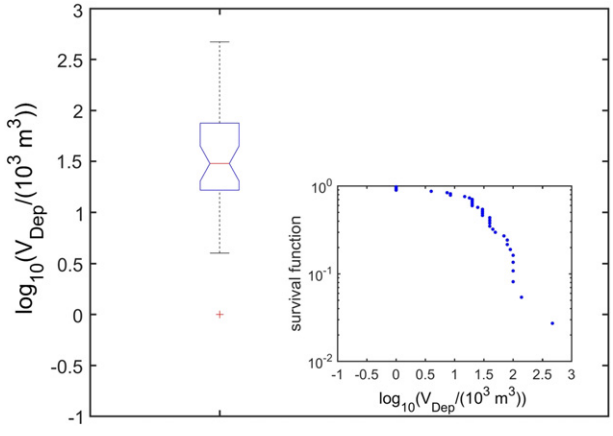

Fig. 4. Observed deposition volume, $\log_{10}(V_{Dep}/V_0)$. The median is shown by the red central mark, the 25th–75th percentile as edges of the blue box, and the whiskers extend to the most extreme data points not considered outliers. The notched area signifies a 95% confidence interval for the median. The inset plots the corresponding survival function. (For references to color in this figure, the reader is referred to the web version of this article.)

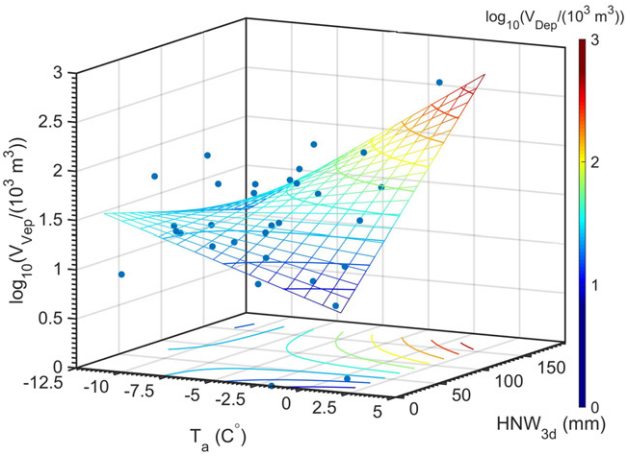

Fig. 5. Observed deposition volume, $\log_{10}(V_{Dep}/V_0)$, in relation to air temperature, T_a, and three-day new-snow water equivalent, HNW_{3d}. The surface plot and the contour lines depict the linear regression model. Colors give the order of magnitude of the deposition volume. (For interpretation of the references to color in this figure legend, the reader is referred to the web version of this article.)

Looking at the location of the α point, the data suggests a nominal return period of 10 to 30 years for the Ryggfonn path and looking at the α-1 point, a return period of about 50 to 100 years. Regarding these return periods, one should, however, keep in mind that these observations include artificially triggered avalanches, which otherwise may not have released. Therefore, the return periods may be slightly biased.

Following the main track, we are able to determine the runout probability ("survival probability") for all avalanche events that reached the runout area (i.e. surpassed at least the elevation of the transmission line). A plot of the runout probability vs. horizontal distance, x, is shown in the inset of Fig. 6. On the flat area downstream of the dam, the runout probability decreases nearly exponentially. In our case, a factor 10 in runout probability corresponds to approximately a difference of 230 m in runout distance.

A more detail discussion on runout probability and the efficiency of the catching dam can be found in Gauer et al. (2009) or Faug et al. (2008).

4.3. Mean retarding acceleration based on energy considerations

Gauer et al. (2010b) tried to link observation of "extreme runouts" (i.e. avalanches with return periods of the order of 100 years) with some dynamical parameters. To this end, they used the concept of the mean retarding acceleration, which is a measure for the energy dissipation per unit mass (it also accounts for effects due to mass entrainment, but does not employ assumptions on the rheology), and is given by

$$|\langle a_{ret} \rangle| = \frac{gH}{S}. \tag{1}$$

The equation basically states that the potential energy, gH, where H is the total fall height of the avalanche and g the gravitational acceleration, is dissipated along the total travel distance, S (measured along the track), at a mean rate of $|\langle a_{ret} \rangle|$. Here, we use the $\langle \bullet \rangle$ operator to indicate that we consider a mean value along the track. It is

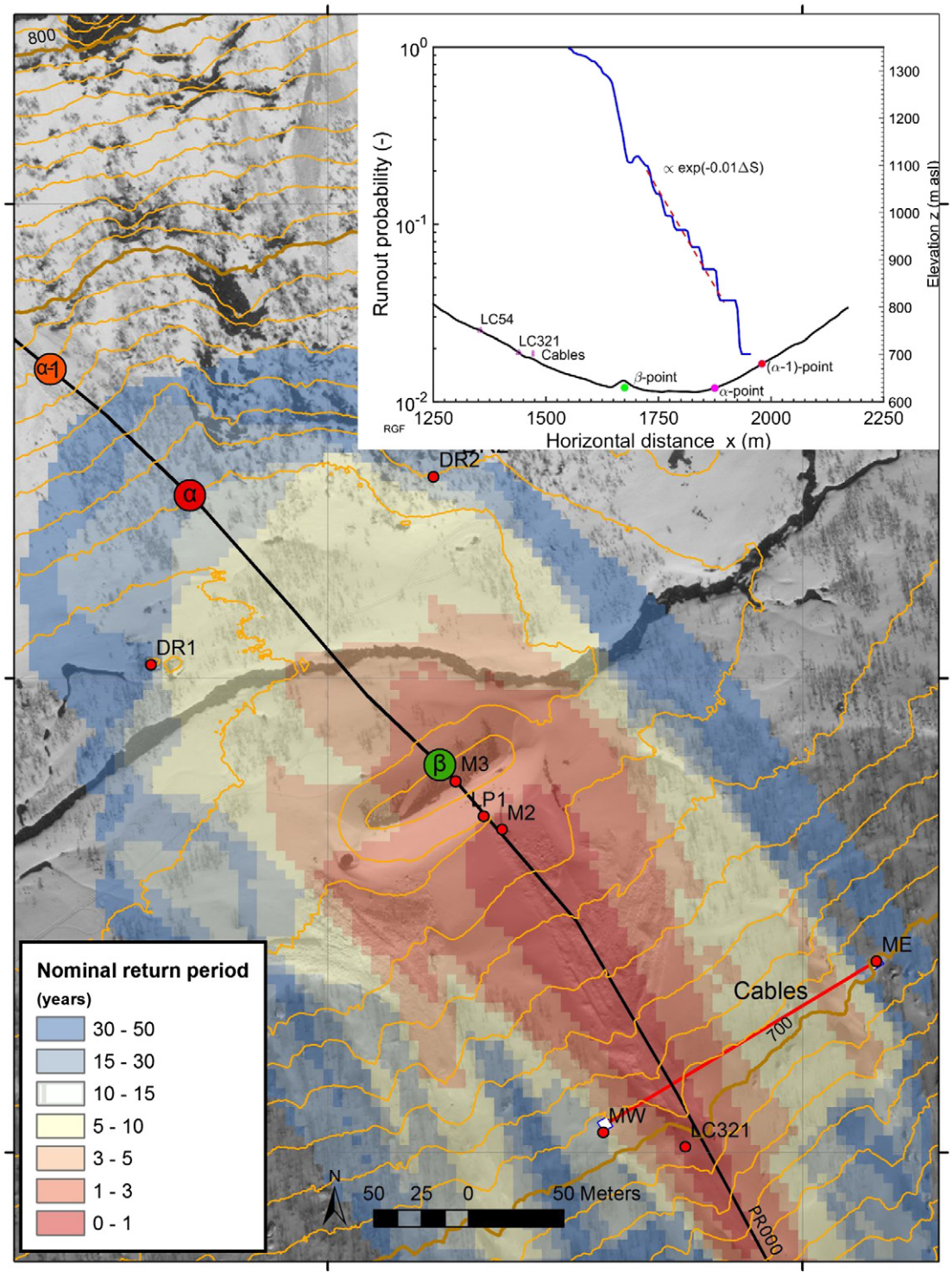

Fig. 6. Nominal return period for a raster point to be reached by an avalanche / covered by deposits (10 m contour lines). For comparison the β and the so-called α, and α-1 points of the well known α-β model (Lied and Bakkehøi, 1980) are shown. The small red dots mark some of the instrumented locations. The inset shows the runout probability along the main track for avalanches that surpassed the transmission line. The dashed line provides a reference with exponential decay. (For interpretation of the references to color in this figure legend, the reader is referred to the web version of this article.)

reasonable to assume that $\langle a_{ret} \rangle$ depends on the ambient conditions, like topography or snow and weather conditions.

Gauer et al. (2010b) found that $\langle a_{ret} \rangle$ for a data set of several hundred avalanches is linearly correlated with the $g\sin\beta$ (correlation coefficient $\rho_{xy} \approx 0.82$):

$$|\langle a_{ret} \rangle_\alpha| \approx g\,(0.82 \sin\beta + 0.052), \qquad (2)$$

where we use the subscript α to mark the link to the α-β model (Lied and Bakkehøi, 1980).

Fig. 7 shows the "survival probability" of $\langle a_{ret} \rangle$ for 37 observed avalanches at Ryggfonn. Considering that lower absolute values suggest longer runouts, the figure gives some indication of the change in runout probability. In our case, a factor 10 in probability corresponds to $\Delta\langle a_{ret} \rangle / g \approx 0.08$.

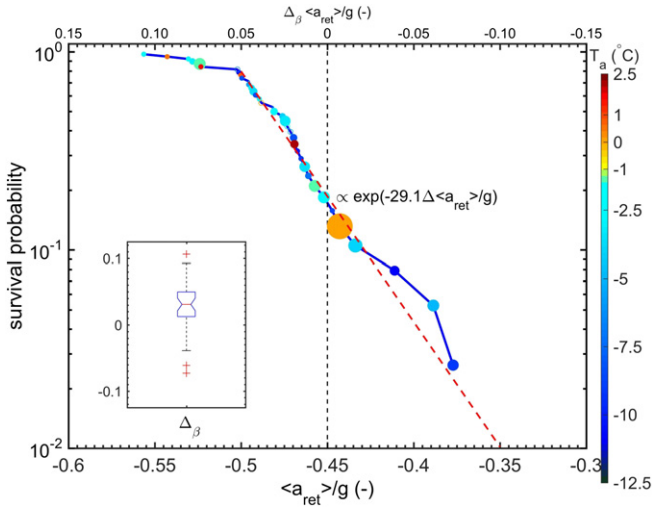

Fig. 7. Survival probability of the retarding acceleration, $\langle a_{ret}\rangle$. The top axis shows $\Delta_\beta\langle a_{ret}\rangle = (\langle a_{ret}\rangle_a - \langle a_{ret}\rangle)$. The size of the marker indicates the relative size of the estimated deposition volume and the marker color reflects the air temperature, T_a. The red dashed line provides a reference with exponential decay. The inset shows a boxplot for $\Delta_\beta\langle a_{ret}\rangle$. The median is shown by the red central mark, the 25th–75th percentile as edges of the blue box, the whiskers extend to the most extreme data points not considered outliers and outliers are marked with a red cross (points larger than $q_3 + 1.5(q_3 - q_1)$ or smaller than $q_1 - 1.5(q_3 - q_1)$, where q_1 and q_3 are the 25th and 75th percentiles). The notched area signifies a 95% confidence interval for the median. (For interpretation of the references to color in this figure legend, the reader is referred to the web version of this article.)

Using Eq. (1) one obtains an estimate of the change in runout length ΔS:

$$\frac{\Delta\langle a_{ret}\rangle}{\langle a_{ret}\rangle} = \frac{\Delta H}{H} - \frac{\Delta S}{S}. \tag{3}$$

Assuming an avalanche that had reached the valley bottom, in which case ΔH becomes approximately zero, then

$$\Delta S \approx \frac{S_0^2}{H_0}\frac{\Delta\langle a_{ret}\rangle}{g}, \tag{4}$$

where H_0 and S_0 are defined by a known reference point. Now using, for example, the β point as reference ($H_0 \approx 900\text{m}, S_0 \approx 1940\,\text{m}, \langle a_{ret0}\rangle/g = \langle a_{ret\beta}\rangle/g \approx 0.46$), we obtain an estimated runout difference that corresponds to factor 10 in probability of $\Delta S \approx 335$ m. This estimate gives a somewhat higher value than that estimated from the direct runout observation above (≈ 230 m). One reason for this difference is probably that the observed runouts are more affected by the presence of the catching dam than reflected by $\langle a_{ret}\rangle$.

That temperature and especially snow temperature may have an influence on the mobility of avalanches has been recognized for a long time. Oechslin (1938) for example distinguished between: “ground avalanches”, “surface avalanches”, and “powder avalanches” in his avalanche velocity observations. Recently, Steinkogler et al. (2014) investigated the influence of snow cover properties on avalanche dynamics in more detail. Also Naaim et al. (2013) put a focus on the correlation between snow characteristics and the parameters of an avalanche model.

In Fig. 8, we show the detrended mean retarding acceleration $\Delta_\beta\langle a_{ret}\rangle$ vs. the air temperature, T_a, of a series of observed avalanches at Ryggfonn, where

$$\Delta_\beta\langle a_{ret}\rangle = \langle a_{ret}\rangle_a - \langle a_{ret}\rangle. \tag{5}$$

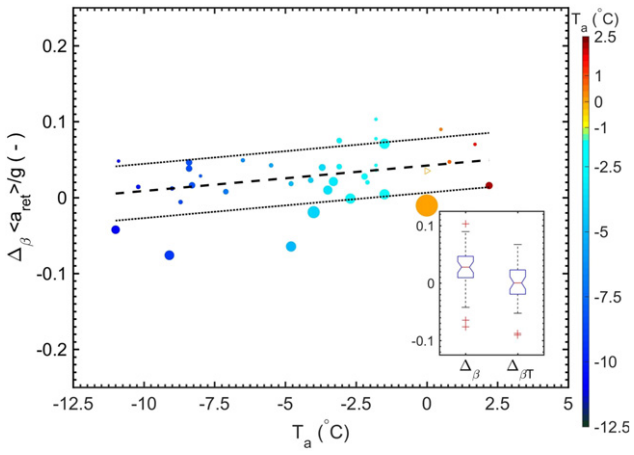

Fig. 8. Detrended mean retarding acceleration, $\Delta_\beta\langle a_{ret}\rangle/g$, vs. the air temperature, T_a. The size of the marker indicates the relative size of the estimated deposition volume and the open triangle depicts one event for which no reliable estimates exist. The marker color reflects the air temperature, T_a. The dashed lines indicate the linear trend and the dotted lines mark the $\pm\sigma$ range. The inset shows boxplots for $\Delta_\beta\langle a_{ret}\rangle/g$ and $\Delta_{\beta T}\langle a_{ret}\rangle/g$. Box plot features are the same as in Fig. 7. (For interpretation of the references to color in this figure legend, the reader is referred to the web version of this article.)

Here, a positive sign of $\Delta_\beta\langle a_{ret}\rangle$ implies higher retardation and consequently shorter runout distances.

Unfortunately, we do not have sufficient snow temperature measurements from near the Ryggfonn path, which would be more representative for the snow conditions during the event. Instead, we use here and in the following, the mean air temperature, T_a, of a 48 h period around the avalanche event as an indicator for the snow conditions. Then again, air temperature series are more often available or obtainable than snow temperature measurements when it comes to estimate return periods for hazard zoning, for example. Also, the temperature of the ambient air may affect the avalanche if air is entrained. The temperature data are derived from measurements from Fonnbu and supplemented by data from **seNorge**. The elevation of Fonnbu (950 m a.s.l.) corresponds roughly to the middle section of the Ryggfonn path. Just as a reminder, the common averaged atmospheric lapse rate of 0.65 °C /100 m implies a temperature difference of approximately 6 °C between the release and the runout area. Therefore, avalanches may have started as dry-snow avalanche and run into moist snow in the valley.

Seemingly, there is a slight trend that $\Delta_\beta\langle a_{ret}\rangle$ increases as the air temperature increases (correlation coefficient $\rho_{xy,z} \approx 0.39$, where $\rho_{xy,z}$ is the partial correlation controlling for V_{dep}), that means, the runout length is expected to decrease. However, the boxplot in the inset shows that the reduction of the spreading is rather low (i.e. the reduction of the inter quartile range, IQR $= q_3 - q_1$). In addition, the trend is less significant than the following one.

In the next step, Fig. 9 presents the detrended mean retarding acceleration $\Delta_{\beta T}\langle a_{ret}\rangle$ vs. the order of magnitude of the estimated deposition volume, $\log_{10}(V_{Dep}/V_0)$. In this case, $\Delta_{\beta T}\langle a_{ret}\rangle$ shows a decreasing trend with increasing deposition volume (correlation coefficient $\rho_{xy,z} \approx -0.58$), which means large avalanches tended to have longer runouts. If we assume that a possible correlation between T_a and $\log_{10}(V_{Dep}/V_0)$ can be neglected ($\rho_{xy} \approx -0.12$), we obtain the linear regression model:

$$\Delta_\beta\langle a_{ret}\rangle/g = \Delta_{\beta 0}\langle a_{ret}\rangle/g + b_1 T_a + b_2 \log_{10}(V_{Dep}/V_0), \tag{6}$$

where $\Delta_{\beta 0}\langle a_{ret}\rangle/g = 0.0085$, $b_1 = 0.0034\,^\circ\text{C}^{-1}$, and $b_2 = -0.033$. The comparison of the boxplots in Figs. 8 and 9 indicates a marked reduction of the spreading.

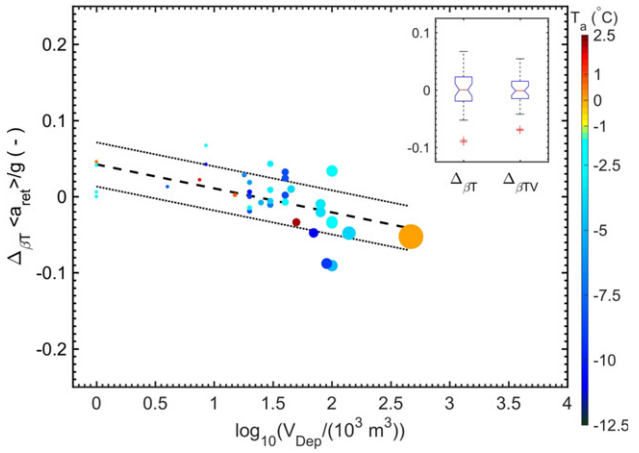

Fig. 9. Detrended mean retarding acceleration, $\Delta_{\beta T}\langle a_{ret}\rangle/g$, vs. the order of magnitude of the deposition volume, $\log_{10}(V_{Dep}/V_0)$. The size of the marker indicates the relative size of the estimated deposition volume and the marker color reflects the air temperature, T_a. The dashed lines indicate the linear trend and the dotted lines mark the $\pm\sigma$ range. The inset shows boxplots for $\Delta_{\beta T}\langle a_{ret}\rangle/g$ and $\Delta_{\beta TV}\langle a_{ret}\rangle/g$. Box plot features are the same as in Fig. 7. (For interpretation of the references to color in this figure legend, the reader is referred to the web version of this article.)

Using Eq. (4) with the β-point as reference one can get an impression of the contributions of the various terms to the change in runout length ΔS. For instance, one could expect an increase in runout length $\Delta S \approx 140$ m per 10 °C temperature decrease—or looking at Fig. 7, corresponding to a reduction in probability of approximately a factor 0.4. The same difference could be expected for an increase of one order of magnitude in deposition volume.

Unfortunately, the deposition volume is not a predictive variable and is instead a rather dynamic value so that it cannot be used directly to estimate the runout distance. The deposition volume depends largely on the entrainment of mass along the track.

A better predictor (i.e. a value that could be estimated a-priori) might be the ratio between release mass and the averaged track width, shown in Fig. 10. The partial correlation coefficient however is lower in this case ($\rho_{xy,z} \approx -0.42$, controlling for T_a).

Of course, one should keep in mind that a correlation does not necessarily imply a causality.

4.4. Mass balance

To give an impression of how the deposited mass relates to the released mass, boxplots of the release mass and deposit mass for a sample of 28 avalanches are presented in Fig. 11. For these avalanches, sufficient observations on the release area/volume and densities were available to obtain estimates of the release mass, M_{rel}, the deposit mass, M_{dep}, and on the entrained mass, $M_{ent} = M_{dep} - M_{rel}$. Here, we employed a Monte Carlo approach for calculating M_{rel}, M_{dep}, M_{ent}, and M_{rel}/M_{dep} to include base data uncertainty. To this end, we used probability distributions that reflect the uncertainty of the base data, which are the release and deposition volume, the snow density in the release area/path and the density of the deposit. Based on these distributions we simulated probability distributions for our response variables M_{rel}, M_{dep}, M_{ent}, and M_{rel}/M_{dep}. Fig. 11 shows that entrainment plays an important role for the mass balance—on average entrainment contributed to about 60% of the deposit. Or in other words, on average, the mass increased by a factor of approximately 3 to 3.5 in these events, although the spreading is considerable, which is partly caused by the differences in the overrun area during the descent. To give a more informative value, Fig. 12 provides the corresponding entrainment per square meter projected area of the track and the corresponding vertical erosion depth. The observed erosion depths are comparable to those measured by Sovilla (2004) or Sovilla et al. (2001). One should, however, keep in mind that these values are averages and are not necessarily uniform along the track. Furthermore, it is reasonable to assume that the erosion process is influenced by the snowpack conditions. Fig. 13 displays the entrainment, M_e', per square meter vs. air temperature, T_a, and three-day new-snow water equivalent, HNW_{3d}. The data suggest higher entrainment with increasing temperature (correlation coefficient $\rho_{xy,z} \approx 0.5$, where $\rho_{xy,z}$ is the partial correlation controlling for HNW_{3d}). The correlation between M_e' and the new-snow water equivalent is rather low ($\rho_{xy,z} \approx 0.3$, where $\rho_{xy,z}$ is the partial correlation controlling for T_a).

A slightly better correlation seems to exist between entrained mass, M_e', per square meter, the air temperature, T_a, and release mass, M_{rel}, per mean track width, w, which is shown in Fig. 14.

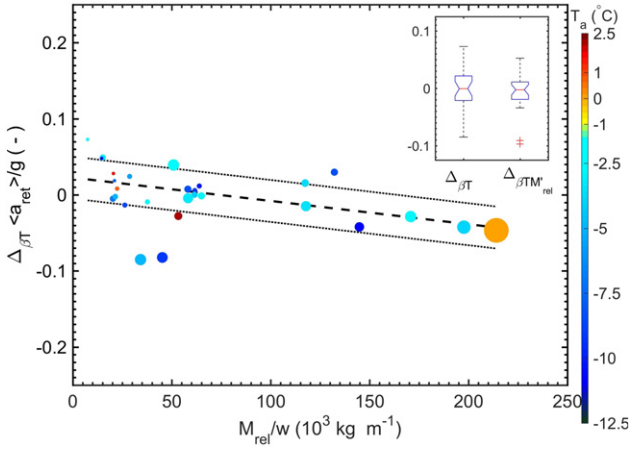

Fig. 10. Detrended mean retarding acceleration, $\Delta_{\beta T}\langle a_{ret}\rangle/g$, vs. release mass, M_{rel}, per mean track width, w. The size of the marker indicates the relative size of the approximated deposition volume and the marker color reflects the air temperature, T_a. The dashed lines indicate the linear trend and the dotted lines mark the $\pm\sigma$ range. The inset shows boxplots for $\Delta_{\beta T}\langle a_{ret}\rangle/g$ and $\Delta_{\beta T\ M'_{rel}}\langle a_{ret}\rangle/g$. Box plot features are the same as in Fig. 7. (For interpretation of the references to color in this figure legend, the reader is referred to the web version of this article.)

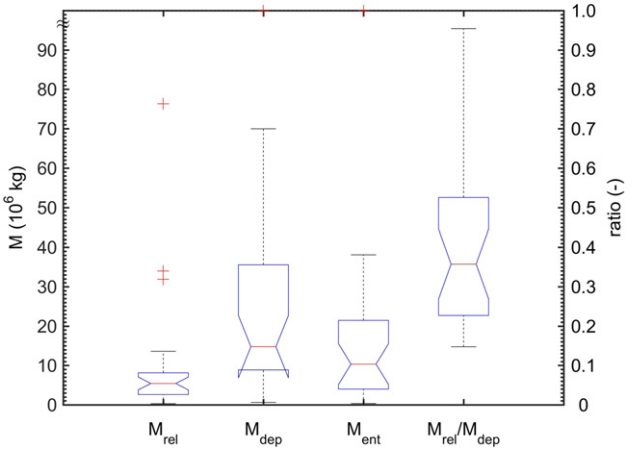

Fig. 11. Released mass, M_{rel}, deposited mass, M_{dep}, entrained mass, M_{ent}, for a sample of 28 avalanches. The right axis ordinate shows the corresponding ratio M_{rel}/M_{dep}. The median is shown by the red central mark, the 25th–75th percentile as edges of the blue box, the whiskers extend to the most extreme data points not considered outliers and outliers are marked with a red cross. The notched area signifies a 95% confidence interval for the median. (For references to color in this figure, the reader is referred to the web version of this article.)

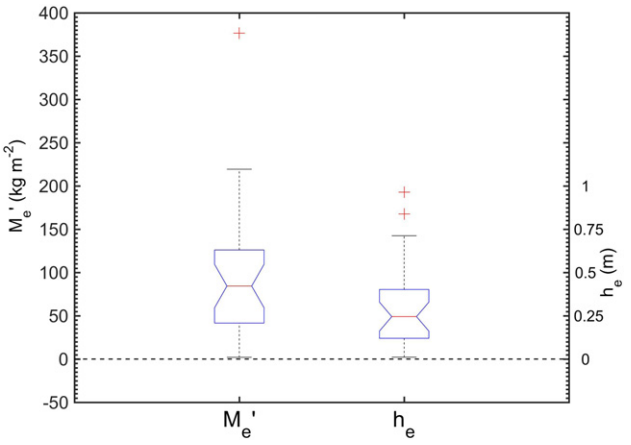

Fig. 12. Entrainment, M_e', per square meter projected area of the impacted track (excluding the release area). The right axis ordinate shows the corresponding averaged vertical erosion depth, h_e. Box plot features are the same as in Fig. 11.

In this case, the reduction in unexplained variance is about 0.65. The partial correlation coefficients between pairs of variables in M_e' and $[T_a, M_{rel}/w, \mathrm{HNW}_{3d}]$, while adjusting for the remaining ones are: [0.43, 0.47, −0.07]. The later actually suggests that HNW_{3d} is negligible to a first approximation. The corresponding linear regression model using robust fitting is

$$M_e' = M_{e0}' + b_1 T_a + b_2 M_{rel}/w + b_3 T_a M_{rel}/w, \tag{7}$$

with $M_{e0}' = 37.5\,\mathrm{kg\,m^{-2}}$, $b_1 = 1.71\,\mathrm{kg\,m^{-2}{}^{\circ}C^{-1}}$, and $b_2 = 1.71\,\mathrm{m^{-1}}$ and $b_3 = 0.12^{\circ}\mathrm{C^{-1}\,m^{-1}}$.

In this case, M_{rel}/w is the most significant predictor variable. However, the amount of available data is still too low and uncertain to draw definite conclusions.

4.5. Front velocity observations

In several cases, it was possible to derive avalanche front velocities along the track or at least extended parts of it using time lapse photos or videos (for more detailed information on these events see e.g. Gauer, 2012, 2013, 2014). In recent years, the velocity was also measured using pulsed Doppler radar (Gauer et al., 2007b, 2008b).

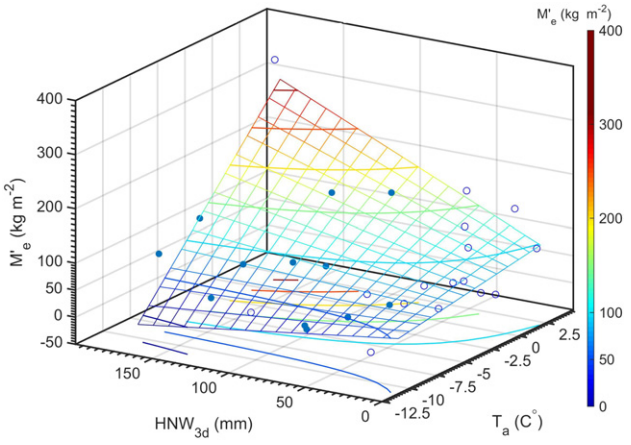

Fig. 13. Entrainment, M_e', in relation to air temperature, T_a, and three-day new-snow water equivalent, HNW_{3d}. Open markers indicate a higher uncertainty. The surface plot and the contour lines depict the linear regression model. Colors reflect the entrainment, M_e'. (For references to color in this figure, the reader is referred to the web version of this article.)

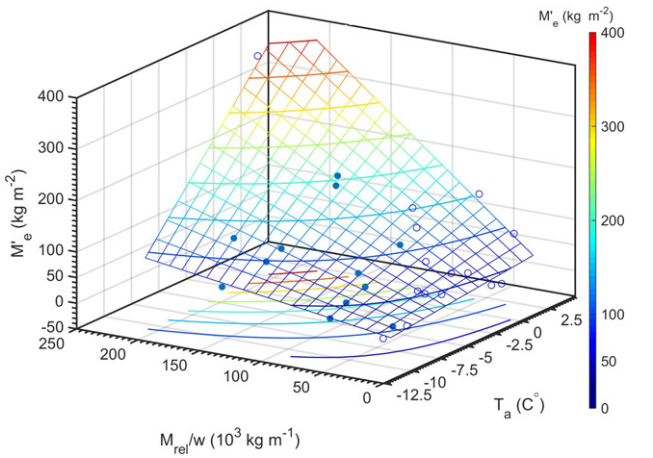

Fig. 14. Entrainment, M_e', in relation to air temperature, T_a, and release mass, M_{rel}, per mean track width, w. Open markers indicate a higher uncertainty. The surface plot and the contour lines depict the linear regression model. Colors reflect the entrainment, M_e'. (For interpretation of the references to color in this figure legend, the reader is referred to the web version of this article.)

Fig. 15 presents the mean observed front velocity along the track and the corresponding $\pm\sigma$ range derived from the available measurements. In addition, the observed maximum speed is also shown. However, it should be noted that the maximum does not belong to a single event, which is partly due to the lack of data in the upper part of the track from one of the major events. In all shown cases, the avalanche reached at least the position of LC54. The plot is supplemented by a distribution of all front velocities, U_{LC}, that could be derived from the timing of the impact between sensor pairs at LC54 and LC321 and a distribution of the front velocity, U_b, at the base of the catching dam. These distributions also include measurements from natural releases and show therefore a slightly different behavior—especially in front of the dam, as the natural releases involved more avalanches that stopped in the area upstream of the dam. Field campaigns are usually undertaken when the probability to observe a decent size avalanche is high. This “human factor” may cause a bias in the observations.

Fig. 15 suggests quite a bit of variation in the flow behavior influenced by varying ambient conditions. How the ambient conditions may influence the avalanche front velocity is presented in Fig. 16. It shows the observed front velocity U_{LC} vs. T_a and versus the three day new snow water equivalent, HNW_{3d} (vertical planes). The bottom plane shows the corresponding scatter plot of HNW_{3d} vs. T_a.

Although there is a considerable scatter, Fig. 16 suggests that:

- U_{LC} decreases with increasing air temperature $T_a (\rho_{xy,z} \approx -0.32)$; — possibly caused by increased wetness of the snowpack and larger clod size.
- U_{LC} increases with the amount of new snow $\mathrm{HNW}_{3d} (\rho_{xy,z} \approx 0.15)$.

Taken for themselves each of these trends are significant and they are consistent with the observed mean retarding accelerations (see Section 4.3).

However, the background story might be more complicated, as for example T_a and HNW_{3d} are seemingly (slightly) correlated. A multiple regression analysis gives

$$U_{LC} = U_{LC0} + b_1 T_a + b_2 \mathrm{HNW}_{3d} + b_3 T_a \mathrm{HNW}_{3d} \tag{8}$$

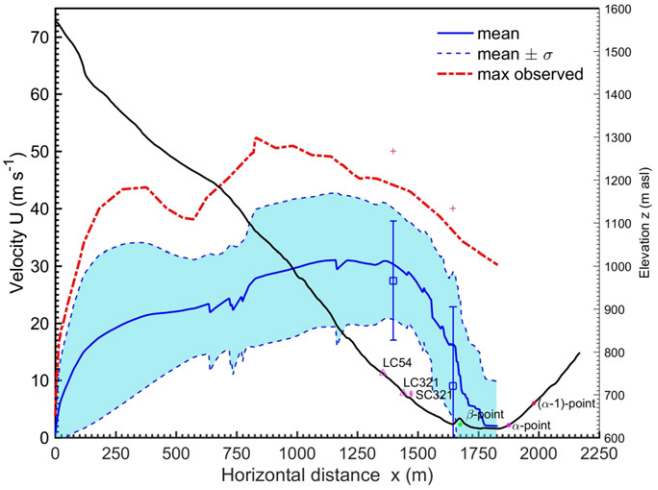

Fig. 15. Front velocity along the track. The blue line shows the mean, the shaded area the $\pm\sigma$ range and the red dashed line the observed maximum derived from observations along the track. In addition, error-bars indicate the distribution of the front velocity U_{LC} measured between LC54 and LC321 and the front velocity U_b at the base of the catching dam. The red crosses mark the measured maxima. (For references to color in this figure, the reader is referred to the web version of this article.)

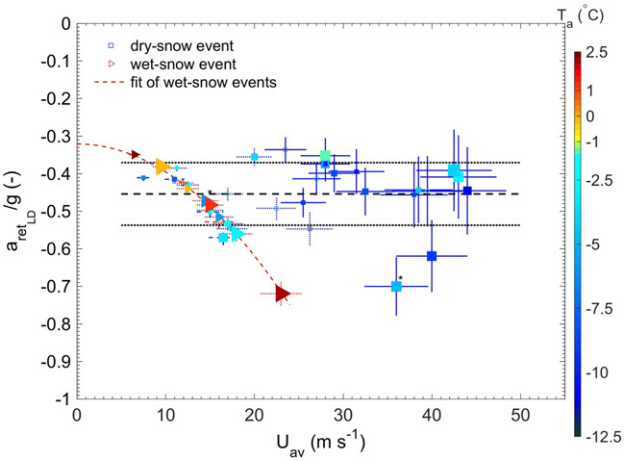

Fig. 17. Retarding acceleration, $a_{ret_{LD}}/g$, between LC and the base of the dam vs. the average speed, U_{av}, along this stretch and with avalanche type as classifier. The dashed line shows the mean value and the dotted lines plot plus or minus one standard deviation for all considered events. The full lines in the error bars mark avalanches that overflowed the dam, dotted-lines mark these that stopped at the dam (20 m from the top), and dashed lines mark these that stopped upstream of the dam. The size of the marker indicates the relative size of the deposition and open markers show those events with unknown volume. The marker color reflects the air temperature, T_a. Two avalanches that occurred before the dam was built are marked with asterisks. (For interpretation of the references to color in this figure legend, the reader is referred to the web version of this article.)

with $U_{LC0} = 23.5\,\mathrm{m\,s^{-1}}$, $b_1 = -0.64\,\mathrm{m\,s^{-1}\,{}^\circ C^{-1}}$, and $b_2 = 0.022\,\mathrm{m\,s^{-1}}$ (mm w.e.)$^{-1}$ and $b_3 = -0.004\,\mathrm{m\,s^{-1}\,{}^\circ C^{-1}}$(mm w.e.)$^{-1}$. In this case, T_a is the most significant variable.

Velocity measurements including velocities from within the avalanche body can be found in Gauer et al. (2007a,b).

4.6. Retarding acceleration derived from front velocity observations

In Section 4.3, we presented the mean retarding acceleration derived from observation of the runout length. Fig. 17 displays now the mean retarding acceleration, $a_{ret_{LD}}$, for the path section from the midpoint between the steel pylon and the concrete wedge (referred to as LC) to the base of the dam derived from front velocity measurements. In this area, the avalanches usually decelerate and start to stop (see Fig. 15). Here, the retarding acceleration is defined as

$$a_{ret_{LD}} = \frac{U_b^2 - U_{LC}^2}{2\Delta s} - g\sin\bar{\phi}\,, \tag{9}$$

where $\bar{\phi}$ is the mean slope angle of the stretch between LC and the base of the dam. U_b is the velocity at the base of the dam or zero if the avalanche stopped before. Similarly, Δs is the distance between LC and the dam or the distance of the runout measured from LC. In this way, $a_{ret_{LD}}$ gives a measure of the instantaneous value in the runout area, in contrast to $\langle a_{ret}\rangle$ from Eq. (1), which is an average for the whole track. The average speed along this stretch is $U_{av} \approx (U_{LC} + U_b)/2$.

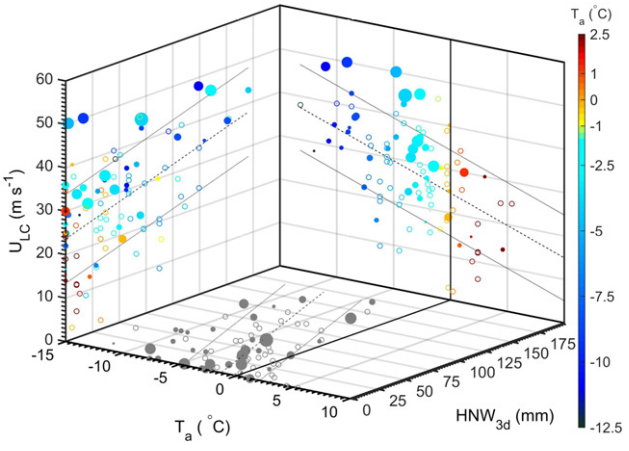

Fig. 16. U_{LC} vs. HNW_{3d} left vertical panel; U_{LC} vs. T_a right vertical panel, and HNW_{3d} vs. T_a. The dashed lines indicate the respective linear trend and the dotted lines mark the corresponding $\pm\sigma$ range. Colors indicate the air temperature and the size of the markers indicates the relative size of the deposition volume. Open markers indicate the events where no volume data are available. (For interpretation of the references to color in this figure legend, the reader is referred to the web version of this article.)

For those avalanches that were classified as dry-snow avalanches (marked as squares), there is no significant correlation between the retarding acceleration, $a_{ret_{LD}}$, and U_{av} (Spearman rank correlation coefficient $\rho_{SR} = 0.06$). In contrast, the Spearman rank correlation for those events classified as wet-snow avalanches (marked as triangles) suggests a relationship (Spearman rank correlation coefficient $\rho_{SR} > 0.9$). These events can be fitted to a parabola $a_{ret_{LD}}/g = -7.4\times10^{-4}\,U^2 - 0.32$, as indicated in the figure. Incidentally, all dry-snow events with $U_{av} < 20$ m s^{-1} are close to this curve too. This distinction may indicate two different flow regimes (for explanation of flow regimes see, e.g., Gauer et al., 2008a) with a transition occurring at velocities of about 20 m s^{-1} in our case, but temperature may also influence the transition.

The boxplots in Fig. 18 give an overview of the retarding accelerations $a_{ret_{LD}}$ for different event types, that is the events are classified as:

- all dry-snow avalanche (dry);
- only those dry-snow avalanches that reached the dam crown or surpassed it (topped);
- wet-snow avalanche (wet);
- all avalanches combined.

For comparison, the mean retarding acceleration, $\langle a_{ret}\rangle$, as well as the averaged retarding acceleration derived from front velocity

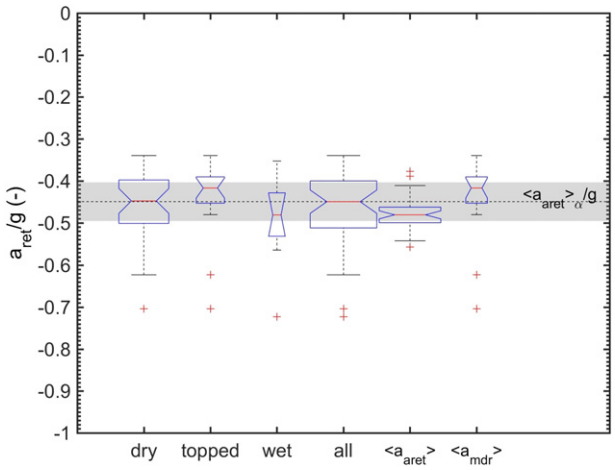

Fig. 18. Comparison of derived retarding accelerations, $a_{ret_{LD}}$, based on front velocity measurements for different event types. In addition, the mean retarding acceleration, $\langle a_{ret}\rangle$, based on runout observation s (see Section 4.3) as well as the averaged retarding acceleration, $\langle a_{mdr}\rangle$, based on a simple energy model approach (see for details Gauer, 2013) are shown. The width of the box indicates the relative sample size ($N_{total} = 40$); the median is shown by the red central mark, the 25th–75th percentile as edges of the blue box, the whiskers extend to the most extreme data points not considered outliers and outliers are marked with a red cross. The notched area signifies a 95% confidence interval for the median. The dashed line corresponds to the retarding acceleration derived from α-β model (cf. Eq. (2)) and the shaded area is the corresponding $\pm\sigma$ range. (For references to color in this figure, the reader is referred to the web version of this article.)

observations along the full track and based on a simple energy model approach (see for details Gauer, 2013) are included and marked $\langle a_{mdr}\rangle$. Although derived by different means and partly biased due to incomplete data, the values seem to be consistent. The data are also in accordance with instantaneous values from within the avalanche derived from pulsed Doppler radar measurements (cf. Gauer et al., 2007a,b). As additional reference, $\langle a_{ret}\rangle_\alpha$ derived from α-β model (Gauer et al.,2010b; Lied and Bakkehøi,1980) and the corresponding $\pm\sigma$ range are given in Fig. 18. At this point it is worthwhile to mention that the spreading for the Ryggfonn events is primarily caused by the ambient conditions at the time, whereas the variance

Fig. 19. Load plates LC1 (top) and LC2 mounted on the concrete wedge after a wet-snow avalanche event. LC3 is covered by deposition (Avalanche event 1991-03-20).

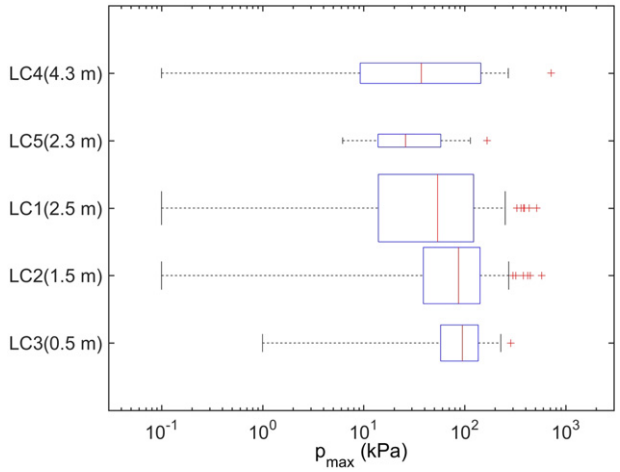

Fig. 20. Measured maximum pressure. Note the log-scale. The width of the box indicates the relative number of measurements with a maximum number of 73 measurements. Numbers in parentheses give the height of the midpoint of the plates above ground.

in the α-β model data is, supposedly, influenced to a large degree by the diversity of the path topographies and vegetation cover and only secondarily by the ambient conditions.

4.7. Impact pressure

Avalanche risk is a function of the impact pressure, which can be regarded as a measure of the destructiveness. As early as 1983, a concrete wedge was installed at the test site (LC321, see Fig. 19) and was equipped with load plates to measure pressure time series. In 2001, two additional load plates were mounted at the present-day pylon, LC54.

Fig. 20 shows boxplots of the maximum measured impact pressure of all avalanches for which more or less reliable data are available. A major problem in this kind of measurements is pre-existing deposition in front of the load plate. The maximum is calculated for a time period of 0.1 s. Short term impacts from snow clods, stones or debris caused higher pressures peaks. Furthermore, the relatively large size of the load plate ($1.2 \times 0.6 = 0.72\ \mathrm{m}^2$) implies a certain spatial average. Nonetheless, impact pressures as high as 720 kPa have been measured.

It is common to express the impact pressure as function of the dynamic pressure (see, e.g., Jóhannesson et al., 2009, and discussion therein)

$$p = C_D^* \frac{\rho U_\infty^2}{2}, \tag{10}$$

where ρ is the flow density and U_∞ the flow velocity upstream of the obstacle. C_D^* is the effective drag factor, which depends on the flow regime and might be split into two terms. One representing the combined dynamic and frictional effect on the obstacle and the other the static force. In this case, C_D^* is given by

$$C_D^* = C_D + \frac{f_s}{\mathbf{Fr}_\infty^2}, \tag{11}$$

where $\mathbf{Fr}_\infty^2 = U_\infty/\sqrt{gh_\infty}$ is the Froude number and h_∞ the upstream flow depth. C_D and f_s are functions depending on the flow regime and the geometry of the flow and obstacle, e.g., on the ratio of particle size to obstacle width.

In Fig. 21, the observed maximum pressures are plotted vs. front velocity, U_{LC}, which is used as reference. It should be noted that the maximum pressures did not necessarily occur at the front and

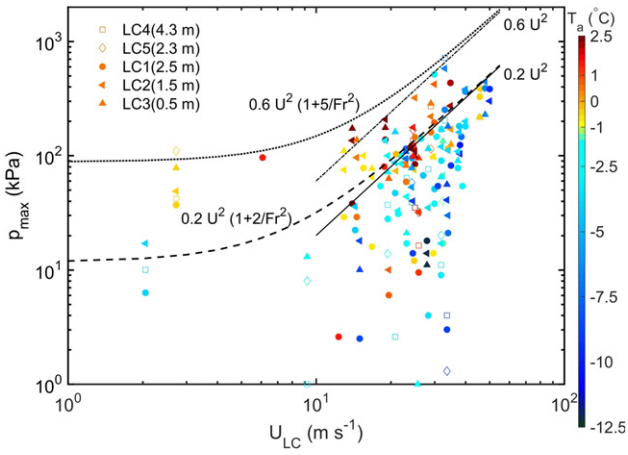

Fig. 21. Measured maximum pressure vs. U_{LC}. Note the log–log-scale. Measurements originate from load plates at LC321 and LC54. Colors indicate the air temperature. Lines may give a kind of upper envelope for the wet- (dotted and dash-dotted) and dry-snow events (dashed and solid), respectively. (For interpretation of the references to color in this figure legend, the reader is referred to the web version of this article.)

that the velocity within the avalanche might be significantly different/lower than in the frontal part, especially in the case of wet-snow avalanches. Therefore, the velocity here should only be regarded as a weak indication of the flow state. Nevertheless, to give some impression how the measurements relate to Eq. (10), the figure shows pairs of lines with parameters, which could be representative for wet- or dry-snow avalanches and which are intended to give an upper envelope. We do not have direct flow height observations to calculate the Froude number. Therefore, we use an estimate for the flow height based on reported flow heights (cf. Gauer, 2014, Table 2) and on the estimate of the mean mass per square meter footprint (see Section 4.9). In either case, an error of factor two in the flow height estimate or in the density estimate, respectively, will reduce to a factor $\sqrt{2}$ in the estimation of the Froude number.

A more detailed discussion on the factor C_D and its dependency on avalanche type and velocity can be found, e.g., in Gauer et al. (2007a, 2008b) or in Sovilla et al. (2008a,b), Baroudi et al. (2011), and Faug (2013).

Fig. 22. View from the Y-mast (now LC54) down to the catching dam and the transmission line assembly after the avalanche event 1989-03-04. The cables were 4 m apart and their diameters were ø 34 mm. The concrete wedge (LC321) is the snow covered hump just left of the mast.

4.8. Pressure on transmission line cables

At an early stage, the Ryggfonn test site was equipped with a transmission line assembly (see Fig. 22). Although only a limited set of data could be obtained, the data are valuable as no comparable data exist. They can be informative for engineers involved in planning of power lines or cable cars.

For the analysis, we assume that the measured maximum tension force, F_m, in the cables can be directly related to the maximum impact pressure of the avalanche or powder cloud onto the cables. Fig. 23 gives an overview of the measured maximum pressure F_m/A on the cables, where A is the projected area of a cable. As can be expected, there is a marked decrease with increasing height above the ground. As reference, a line representing an exponential decrease with a rate factor $e_c = -0.21\ \mathrm{m}^{-1}$ is shown. The maximum pressures reached approximately 65, 40, and 22 kPa on the lower, middle and upper cable, respectively.

It should be mentioned that in all events the avalanche caused flutter in the transmission lines/of the assembly as whole.

Fig. 24 presents the vertical profiles of $2F_m/\left(AU_{LC}^2\right)$. As a reference, the corresponding value at the upper load plate, LC1, at the concrete wedge is also shown. Assuming that the maximum tension force can be expressed by

$$F_m = C_D\,\rho\frac{(c_1\,U_{LC})^2}{2}\,A, \tag{12}$$

the profiles in the figure give some indications for the combination of $C_D\,\rho\,c_1^2$ and its decrease with height. Here, ρ is the flowing density and c_1 is a parameter describing the vertical velocity profile. C_D is the drag coefficient, which may depend on the flow regime and geometries, such as the ratio of particle size to cable diameter (c.f. Bharadwaj et al., 2006; Chehata et al., 2003). In all events, a marked decrease with height is observed. As a first guess, it might be reasonable to assume an exponential decrease. In this case, one notices that the absolute value of the rate factor decreases with increasing velocity. That means $C_D\,\rho\,c_1^2$ decreases slower with increasing avalanche velocity, which seems reasonable considering a turbulent flow. There might be one exception, however, in which case $C_D\,\rho\,c_1^2$ was already small at the lowest cable and one could imagine a rather dilute homogenous cloud.

Assuming a pronounced velocity profile with significantly slower velocities higher up in the powder cloud ($c_1 < 1$) would imply a slower decrease of $C_D\rho$ with height, which seems less intuitive.

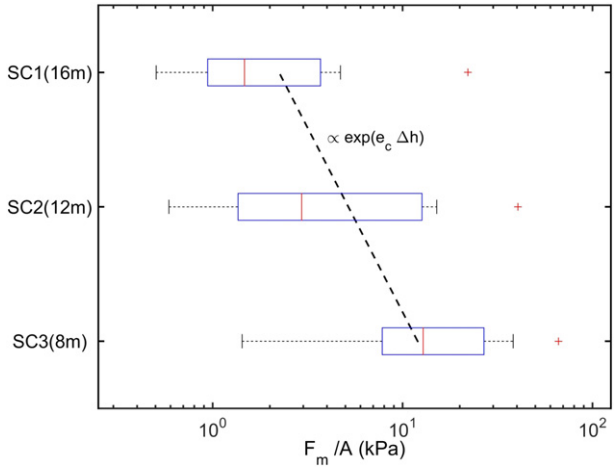

Fig. 23. Maximum pressure on cable. Note the log-scaling of the abscissa. As reference, a line representing an exponential decrease with a rate factor $e_c = -0.21\ \mathrm{m}^{-1}$ is shown. Numbers in parentheses give the respective mounting height above ground.

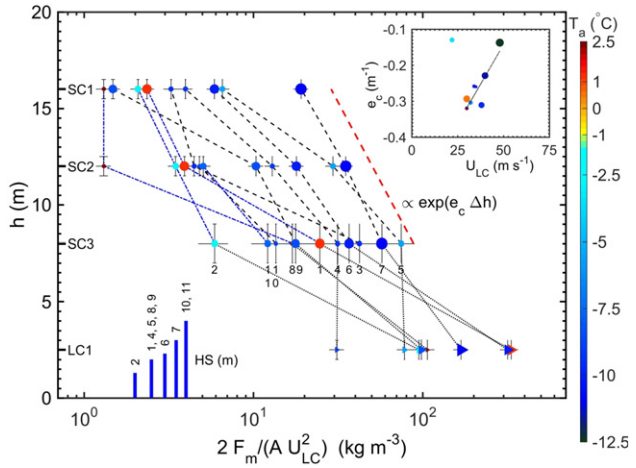

Fig. 24. Vertical profiles of $2F_m/(AU_{LC}^2)$. The red dashed line gives a reference indicating an exponential decrease with a rate factor $e_c = -0.14\,\mathrm{m}^{-1}$. The inset shows the rate factor e_c vs. U_{LC}. Colors reflect the air temperature and the size of the markers gives an indication of the relative size of the avalanche volume. (•) shows measurements at the transmission line and (▲) with the load plate LC1. Bars mark the approximate snow depth under the transmission line before the events, which are given by numbers. (For interpretation of the references to color in this figure legend, the reader is referred to the web version of this article.)

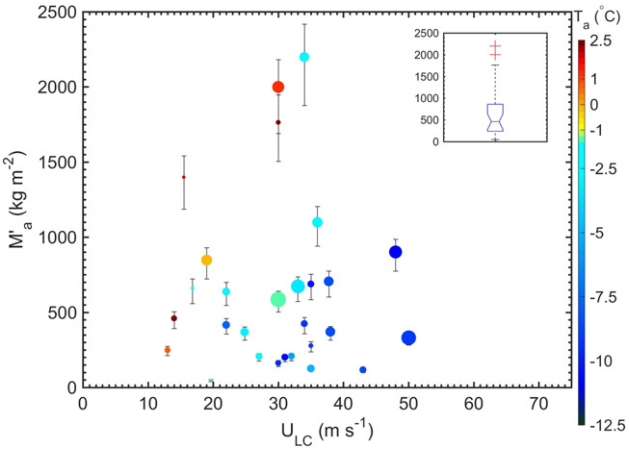

Fig. 25. Mean mass, M_a', per square meter footprint. Colors reflect the air temperature and the size of the markers gives an indication of the relative size of the avalanche volume. Bars show the interquartile range of the respective estimate. The inset shows a boxplot of M_a'. (For interpretation of the references to color in this figure legend, the reader is referred to the web version of this article.)

Taking an effective C_D of approximately 1 to 4, the measurements suggest a flowing density in the range of 1 to 100 kg m^{-3} within the cloud that hit the cables—decreasing with height.

4.9. Mean mass per square meter footprint

Unfortunately, we do not have flow height or density measurements. However, using the estimates for the mass of the deposition, the time of passage, t_a at the concreted wedge (LC321) as well as for the velocity U_{LC} and avalanche width, w, it is possible to gain a rough estimate of the mean mass per square meter footprint of the avalanche:

$$M_a' = \int_0^{h_f} \rho(z)dz \approx f_c \frac{M_{dep}}{U_{LC}\ t_a\ w}, \tag{13}$$

where h_f is the flow height of the avalanche. f_c is a correction factor accounting for the uncertainties in the estimates, e.g., due to varying velocity distributions. We assume f_c to be in the order of 1 ± 0.4. Fig. 25 shows our estimates plotted versus U_{LC}, just to have a reference. We used a Monte Carlo approach involving probability distributions, which reflect our uncertainty of the base data, to quantify the error range of our estimates. The figure suggests a temperature influence with a tendency to lower M_a' for cooler temperatures, which seems reasonable as one would expect higher flow densities for, e.g., wet-snow avalanches. Furthermore, some of the estimates for the dry-snow events suggest flow densities appreciably lower than 300 kg m^{-3}, which is commonly used as flow density in numerical models, using typical flow height estimates (cf. Gauer, 2014, Table 2). This outcome is substantiated by the estimation of density profiles presented in the next section. It is also noteworthy that these estimates are in mutual agreement with estimates that can be derived from the impact pressure measurement on the transmission lines (cf. Fig. 24) or with estimates of the flow densities based on the impact pressure measurements at LC321 (cf. Fig. 21).

4.10. Estimated density profiles

Information on flow densities of avalanches, especially with vertical profiles, is scarce. To gain some insights, we combine our results from the transmission line measurements and our estimates of the mean mass per square meter footprint. If one assumes that an avalanche consists of a core with a height h_0 and density ρ_0 accompanied by a cloud in which the density decreases rather quickly with increasing height as implied in Fig. 24, it is possible to get an estimate of the density profile based on the supposed mean mass, M_a', per square meter footprint (see Section 4.9). To this end, we assume, to a first approximation, that the density in the cloud decreases exponentially as suggested by the observations. In this case, M_a' is given by

$$M_a' = \rho_0\,(h_0 + 1/|e_c|)\,, \tag{14}$$

where e_c rate factor, which depends among other things on the velocity (see inset Fig. 24). While the velocity decreases, $|e_c|$ increases and the density and/or height of the core will increase as expected towards the tail of the avalanche. We deployed the pressure measurements at LC321, to obtain an initial guess on the density ρ_0 and h_0.

Again, we used a Monte Carlo approach to include our uncertainty of the base data. Fig. 26 shows our estimated density profiles for those avalanches for which we have measurements from the transmission line. Here, we focused on the frontal part of the avalanche, in which case the front velocity U_{LC} is a good proxy for the velocity. A comparison with the measurements at the transmission line suggests that the decrease with height may be slightly underestimated in the cases where the air temperature was around zero degree. These cases distinguish themselves also with higher estimates of ρ_0. Nonetheless, the fits seem to comprise the right range as the following comparison suggests.

Fig. 27 shows boxplots of the density estimates based on the tension measurements assuming $c_1 C_D \approx 1$ (see Section 4.8) and for comparison the calculated density according to Eq. (14). Despite the uncertainties behind each of these approaches, the match is reasonably good.

5. Concluding remarks

In this paper, we have presented measurements and observations made at the full-scale avalanche test-site Ryggfonn during the last four decades as well as some derived measures. We focussed

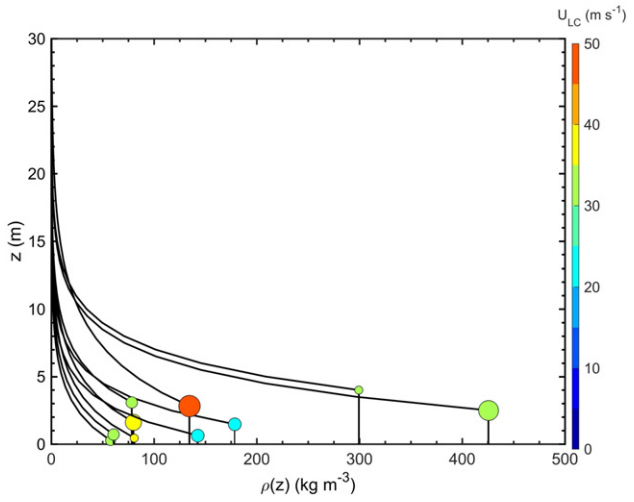

Fig. 26. Estimated density profiles $\rho(z)$ in the frontal part of the avalanche, where z is the height above the sliding surface. Colors reflect the front velocity U_{LC} and the size of the markers gives an indication of the relative size of the avalanche volume. (For interpretation of the references to color in this figure legend, the reader is referred to the web version of this article.)

on runout, velocity, and impact pressure observations as well as on some derived quantities, such as the retarding acceleration or the frontal density. Often, a single measurement/observation may give ambiguous results, however, the combination of results from different measurements—also using different measurement techniques—provides, despite all difficulties, a consistent picture of avalanche dynamics. In this way, our observations reveal, for example, (to a certain extent) the complex dependency of avalanches on the ambient conditions. A fact that was also emphasized by Steinkogler et al. (2014) recently. Furthermore, some of our observations allow estimating the vertical density profile in the frontal part of an avalanche.

Observations and measurements as presented here are important to improve our understanding of avalanche flow, such as the dependency on the ambient conditions, the entrainment of mass, and the development of different flow regimes.

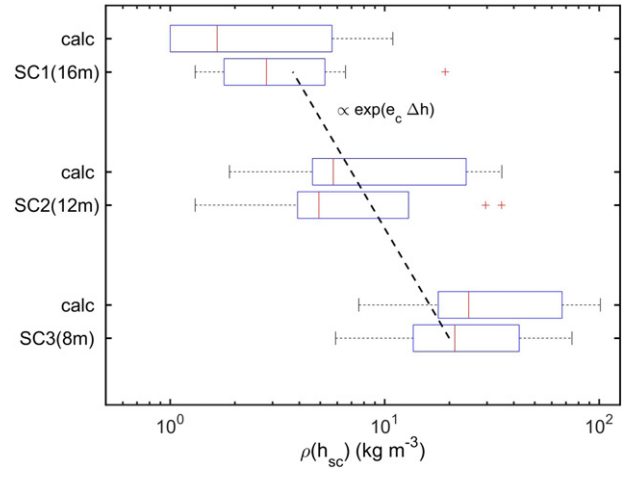

Fig. 27. Estimates of the density range $\rho(h_{SC})$ based on tension measurements with $c_1 C_D \approx 1$ (cf. Section 4.8) and corresponding estimates based on estimates of the mass per square meter footprint (marked with calc). Estimates correspond to the mounting heights of the cables (numbers in parentheses) taking the snow depth into account. Note the log-scaling of the abscissa. As reference, a line representing an exponential decrease with a rate factor $e_c = -0.21\ \mathrm{m}^{-1}$ is shown.

Furthermore, this type of measurements combined with runout observations provides constraints for the development and validation of physically-based numerical avalanche models. These models are increasingly used in the process of hazard zoning to obtain estimates of expected runout distances and impact pressures with varying return periods to delimitate endangered areas in land-use planning (Christen et al., 2010; Naaim et al., 2013; Sampl and Granig, 2009). However, these models are still far from perfect and require a high degree of expert judgment for choosing the required model parameters. Therefore, it is important to have reliable reference data.

Measurements and observations should serve as benchmarks, especially for the probabilistic calibration of numerical models as presented by Fischer et al. (2014, 2015) or for probabilistic design methods such as proposed by Eckert et al. (2009). Probabilistic design methods, however need reliable input distributions of the influencing parameters.

Avalanche measurements as presented here give direct indications of the forces that can be expected in avalanches and the efficiency of certain mitigation measures, like the catching dam at Ryggfonn. In this context, the measurements are directly relevant with respect to avalanche hazard zoning (e.g., Jóhannesson et al., 2009; Lied and Norem, 1986; Norem, 1991). The measurements on the transmission line provided a few unique data that can be informative for engineers involved in planning of power lines or cable cars.

However, further cross-comparisons between different avalanche paths (test sites) are desirable in the future to uncover possible scaling relations. Full-scale avalanche tests are also required for proper interpretation of results from small-scale granular as well as for snow chute experiments. Especially, the complex dependency of avalanches on the ambient conditions, which cannot be reproduced in small-scale experiments, make full-scale experiments invaluable. At the same time, the harsh conditions within an avalanche make measurements a demanding task, the involved costs are very high, and the difficult (non-) reproducibility of the experiments makes the results difficult to interpret. Therefore, a combination of full-scale and small-scale experiments as well as theoretical work is indispensable to understand the flow of avalanches.

Challenges that still exist with respect to avalanche hazard zoning are, among others, the influence of mass entrainment or the transition between different flow regimes and their dependency on the ambient conditions. With a better understanding, estimates of runout distances and their corresponding return periods could be better linked to prevailing snow and weather conditions.

Acknowledgments

Parts of this research were carried out through a snow avalanche research grant to NGI from Norwegian Water Resources and Energy Directorate (NVE). We like to thank all those who were involved in any way in the Ryggfonn Project throughout the years, particularly those in the background such as T. Kvisterøy, K. Tronstad, and E. Lied. We also thank L. McKittrick for his comments to the manuscript and A. Stoffel for some GIS hints. The comments and suggestions of the two reviewers, B. Sovilla and T. Jóhannesson, and the editor-in-chief J. Schweizer were appreciated and helped to improve the paper.

References

Ammann, W.J., 1999. A new Swiss test-site for avalanche experiments in the Vallée de la Sionne/Valais. Cold Reg. Sci. Technol. 30 (1-3), 2–11.

Barbolini, M., Issler, D., 2006. Avalanche Test Sites and Research Equipment in Europe: An Updated Overview. SATSIE Avalanche Studies and Model Validation in Europe.

Baroudi, D., Sovilla, B., Thibert, E., 2011. Effects of flow regime and sensor geometry on snow avalanche impact pressure measurements. J. Glaciol. 57 (202), 277–288.

Bharadwaj, R., Wassgren, C., Zenit, R., 2006. The unsteady drag force on a cylinder immersed in a dilute granular flow. Phys. Fluids 18 (4), 043301(7).

Chehata, D., Zenit, R., Wassgren, C.R., 2003. Dense granular flow around an immersed cylinder. Phys. Fluids 15 (6), 1622–1631.
Christen, M., Kowalski, J., Bartelt, P., 2010. RAMMS: Numerical simulation of dense snow avalanches in three-dimensional terrain. Cold Reg. Sci. Technol. 63, 1–14.
Eckert, N., Parent, E., Faug, T., Naaim, M., 2009. Bayesian optimal design of an avalanche dam using a multivariate numerical avalanche model. Stoch. Env. Res. Risk A. 23, 1123–1141.
Faug, T., 2013. Granular force on objects and correlation length: drag coefficient enhancement in low Froude number flow regimes. POWDERS AND GRAINS 2013: Proceedings of the 7th International Conference on Micromechanics of Granular Media. AIP Conference Proceedings. vol. 1542. pp. 617–621.
Faug, T., Gauer, P., Lied, K., Naaim, M., 2008. Overrun length of avalanches overtopping catching dams: cross-comparison of small-scale laboratory experiments and observations from full-scale avalanches. J. Geophys. Res. Earth Surf. 113, F03009 (1–17).
Fischer, J.T., Fromm, R., Gauer, P., Sovilla, B., 2014. Evaluation of probabilistic snow avalanche simulation ensembles with Doppler radar observations. Cold Reg. Sci. Technol. 97, 151–158.
Fischer, J.T., Kofler, A., Fellin, W., Granig, M., Kleemayr, K., 2015. Multivariate parameter optimization for computational snow avalanche simulation. J. Glaciol. 61 (229), 875–888.
Furseth, A., 2006. Skredulykker i Norge en historisk dokumentar om de mest alvorlige leirskred, snøskred og fjellskred som har rammet oss de siste 500 år. TUN forlag
Gauer, P., 2012. On avalanche (front) velocity measurements at the Ryggfonn avalanche test site and comparison with observations from other locations. Proceedings of the International Snow Science Workshop, 2012, September 16-21, 2012 at the Denaina Center in Anchorage, Alaska. pp. 427–432.
Gauer, P., 2013. Comparison of avalanche front velocity measurements: supplementary energy considerations. Cold Reg. Sci. Technol. 96, 17–22.
Gauer, P., 2014. Comparison of avalanche front velocity measurements and implications for avalanche models. Cold Reg. Sci. Technol. 97, 132–150.
Gauer, P., Breien, H., Issler, D., Kristensen, K., Kronholm, K., Lied, E., Lied, K., 2010. The upgraded full-scale avalanche test-site Ryggfonn, Norway. Proceedings of the International Snow Science Workshop, Lake Tahoe, CA, 2010. pp. 747–752. October, 17-22.
Gauer, P., Issler, D., Lied, K., Kristensen, K., Iwe, H., Lied, E., Rammer, L., Schreiber, H., 2007. On full-scale avalanche measurements at the Ryggfonn test site, Norway. Cold Reg. Sci. Technol. 49 (1), 39–53.
Gauer, P., Issler, D., Lied, K., Kristensen, K., Sandersen, F., 2008. On snow avalanche flow regimes: inferences from observations and measurements. Proceedings of the International Snow Science Workshop 2008, September 21-27, Whistler, British Columbia, Canada. pp. 717–723.
Gauer, P., Kern, M., Kristensen, K., Lied, K., Rammer, L., Schreiber, H., 2007. On pulsed Doppler radar measurements of avalanches and their implication to avalanche dynamics. Cold Reg. Sci. Technol. 50, 55–71.
Gauer, P., Kristensen, K., 2004. Avalanche studies and model validation in Europe, SATSIE: Ryggfonn measurements Winter 2002/2003 and 2003/2004. NGI Report 20021048-5. Norwegian Geotechnical Institute, Sognsveien 72, N-0806 Oslo.
Gauer, P., Kristensen, K., 2005. Avalanche studies and model validation in Europe, SATSIE: Ryggfonn measurements Winter 2004/2005. NGI Report 20021048-8. Norwegian Geotechnical Institute, Sognsveien 72, N-0806 Oslo.
Gauer, P., Kronholm, K., Lied, K., Kristensen, K., Bakkehøi, S., 2010. Can we learn more from the data underlying the statistical $\alpha-\beta$ model with respect to the dynamical behavior of avalanches?. Cold Reg. Sci. Technol. 62, 42–54.
Gauer, P., Lied, K., Kristensen, K., 2008. On avalanche measurements at the Norwegian full-scale test-site Ryggfonn. Cold Reg. Sci. Technol. 51, 138–155.
Gauer, P., Lied, K., Kristensen, K., 2009. Analysis of avalanche measurements out of the runout area of NGI's full-scale test-site Ryggfonn. Cold Reg. Sci. Technol. 57 (1), 1–6.
Gruber, U., Margreth, S., 2001. Winter 1999: a valuable test of the avalanche-hazard mapping procedure in Switzerland. Ann. Glaciol. 32 (1), 328–332.
Heumader, J., 2000. The catastrophic avalanche disaster of Galtuer and Valzur on the 23 and 24. of February 1999. International Symposion INTERPRAEVENT 2000 Villach / Österreich. pp. 397–409.
Innst. S. nr.68, 1973. Innstilling fra industrikomitéen om organisering av snøforsking m.v. i Norge.
Issler, D., 1999. European Avalanche Test-Sites: Overview and Analysis in View of Coordinated Experiments. Mitteilungen 59, Eidgenöss. Inst. Schnee-Lawinenforsch., Davos, Flüelastr 11. CH-7260 Davos.
Jaedicke, J., Kristensen, K., Lied, K., Bakkehøi, S., 2008. Fonnbu, A new (old) platform for snow and avalanche research. Proceedings Whistler 2008 International Snow Science Workshop September 21-27, 2008. pp. 598–603.
Jóhannesson, T., Gauer, P., Issler, D., Lied, K. (Eds.), 2009. The design of avalanche protection dams. Recent practical and theoretical developments. No. EUR 23339 inClimate Change and Natural Hazard Research Series 2. European Commission, Directorate-General for Research ISBN ISSN 978-92-79-08885-8. ISSN 1018-5593.
Kristensen, K., 1996. The Ryggfonn Project: avalanche data from the winters 1991/1992, 1992/1993, and 1993/1994. NGI Report 581200-31. Norwegian Geotechnical Institute.
Kristensen, K., 1997. The Ryggfonn Project: avalanche data from the winters 1994/1995 and 1995/1996. NGI Report 581200-32. Norwegian Geotechnical Institute, Sognsveien 72, N-0806 Oslo.
Kristensen, K., 2001. The Ryggfonn Project: avalanche data from the winters 1996/1997, 1997/1998, 1998/1999 and 1999/2000. NGI Report 581200-33. Norwegian Geotechnical Institute, Sognsveien 72, N-0806 Oslo.
Lied, K., 1984. Earth dams for protection against snow avalanches. Report 58120-4. Norwegian Geotechnical Institute.
Lied, K., Bakkehøi, S., 1980. Empirical calculations of snow-avalanche run-out distance based on topographic parameters. J. Glaciol. 26 (94), 165–177.
Lied, K., Norem, H., 1986. The Ryggfonn project. Forslag til beregning av dimenssjonerende snøskred mot mastekonstruksjoner. Report 58120-16. Norwegian Geotechnical Institute.
Maggioni, M., Freppaz, M., Ceaglio, E., Godone, D., Viglietti, D., Zanini, E., Barbero, M., Barpi, F., Borri Brunetto, M., Bovet, E., Chiaia, B., De Biagi, V., Frigo, B., Pallara, O., 2012. A new experimental snow avalanche test site at Seehore peak in Aosta Valley (NW Italian-Alps) — Part I: preliminary analysis and logistics. Cold Reg. Sci. Technol. 85, 175–182.
McClung, D., Schaerer, P., 2006. The Avalanche Handbook. third ed., The Mountaineers Books, 1011 SW Klickitat Way, Seattle.
Naaim, M., Durand, Y., Eckert, N., Chambon, G., 2013. Dense avalanche friction coefficients: influence of physical properties of snow. J. Glaciol. 59 (216), 771–782.
Norem, H., 1991. Estimating snow avalanche impact pressures on towers. In: Gubler, H.U. (Ed.), Proceedings of a Workshop on Avalanche Dynamics, 14-19 May 1990. Mitt. Eidgenöss. Inst. Schnee- Lawinenforsch. Nr. 48. pp. 42–56.
Norem, H., 1995. The Ryggfonn Project: summary report 1981–1995. Techreport A952-1. Dr. ing. Harald Norem A/S Consultant in Snow Engineering, Molde, Norway.
Norem, H., Kristensen, K., 1985. The Ryggfonn project. Avalanche data from the winter 1982/83. Report 58120-6. Norwegian Geotechnical Institute.
Norem, H., Kristensen, K., 1986. The Ryggfonn project. Avalanche data from the winter 1983/84. Report 58120-7. Norwegian Geotechnical Institute.
Norem, H., Kristensen, K., 1986. The Ryggfonn project. Avalanche data from the winter 1984/85. Report 58120-8. Norwegian Geotechnical Institute.
Norem, H., Kristensen, K., Tronstad, K., 1988. The Ryggfonn project. Avalanche data from the 1986/1987 winter. Report 581200-11. Norwegian Geotechnical Institute.
Norem, H., Kristensen, K., Tronstad, K., 1988. The Ryggfonn project. Avalanche data from the 1987/1988 winter. Report 581200-13. Norwegian Geotechnical Institute.
Norem, H., Kristensen, K., Tronstad, K., 1989. The Ryggfonn project. Avalanche data from the 1988/1989 winter. Report 581200-15. Norwegian Geotechnical Institute.
Norem, H., Kristensen, K., Tronstad, K., 1991. The Ryggfonn project. Avalanche data from the 1989/1990 winter. Report 581200-24. Norwegian Geotechnical Institute.
Oechslin, M., 1938. Lawinengeschwindigkeiten und Lawinenluftdruck. Schweiz. Z. Forstwesen 6, 153–160.
Rapin, F., Ancey, C., 2000. Occurrence conditions of two catastrophic avalanches at Chamonix, France. Proceedings of the International Snow Science Workshop 2000, Bozeman, MT. pp. 509–513.
Saloranta, T.M., 2012. Simulating snow maps for Norway: description and statistical evaluation of the seNorge snow model. Cryosphere 6, 1323–1337.
Sampl, P., Granig, M., 2009. Avalanche simulation with SAMOS-AT. Proceedings of the International Snow Science Workshop, Davos. pp. 519–523.
Sovilla, B., 2004. Field experiments and numerical modelling of mass entrainment and deposition processes in snow avalanches. ETH Zurich, Zurich, Switzerland. Diss. ETH no. 15462
Sovilla, B., Schaer, M., Kern, M., Bartelt, P., 2008. Impact pressures and flow regimes in dense snow avalanches observed at the Vallée de la Sionne test site. J. Geophys. Res. Earth Surf. 113, F01010 (1–14).
Sovilla, B., Schaer, M., Rammer, L., 2008. Measurements and analysis of full-scale avalanche impact pressure at the Vallée de la Sionne test site. Cold Reg. Sci. Technol. 51, 122–137.
Sovilla, B., Sommavilla, F., Tomaselli, A., 2001. Measurements of mass balance in dense snow avalanche events. Ann. Glaciol. 32 (1), 230–236.
Steinkogler, W., Sovilla, B., Lehning, M., 2014. Influence of snow cover properties on avalanche dynamics. Cold Reg. Sci. Technol. 97, 121–131.
The Telegraph, 2015. Avalanches kill more than 300 in Afghanistan. http://www.telegraph.co.uk/news/worldnews/asia/afghanistan/11443833/Avalanches-kill-more-than-180-in-Afghanistan.html.
Thibert, E., Bellot, H., Ravanat, X., Ousset, F., Pulfer, G., Naaim, M., Hagenmuller, P., Naaim-Bouvet, F., Faug, T., Nishimura, K., Ito, Y., Baroudi, D., Prokop, A., Schön, P., Soruco, A., Vincent, C., Limam, A., Héno, R., 2015. The full-scale avalanche test-site at Lautaret Pass (French Alps). Cold Reg. Sci. Technol. 115, 30–41.
Tøndel, I., 1977. Protection of Roads Against Avalanches. University of Trondheim, In Norwegian. Phd thesis.